Wave-based SHM of sandwich structures using cross-sectional waves

Christophe Droz, Olivier Bareille, Jean-Pierre Lainé, Mohamed N Ichchou

Wave-based SHM of sandwich structures using cross-sectional waves

C. Droz[a], O. Bareille[a], J.-P. Lainé[a], M. N. Ichchou[a]

[a]*Ecole Centrale de Lyon, 36 Avenue Guy de Collongue, 69134 Ecully Cedex, France*

Abstract

The identification of structural damage in composite waveguides is a critical issue in aerospace and transportation industries. Frequently, these structures involve periodic patterns or dissipative components which considerably reduce the range, robustness and available bandwidth of ultrasonic structural health monitoring (SHM) techniques. On the other hand, wave-based methods provide more accurate informations on a defect's type, size and location than modal analysis techniques. This paper focuses on a low-frequency wave-based method for structural integrity assessment of complex waveguides. The wave finite element method (WFEM) is employed to compute the dispersion curves of non-standard cross-sectional waves (CSW) exhibiting increased strain energy. The spectral results are used to analyse the diffusion of guided elastic waves through representative localized defects in a laminated sandwich panel. To validate the diffusion model, reflection and transmission coefficients are determined for several wave pulses on typical defects using time-domain virtual experiments and cross-sectional energy acquisition. Results demonstrate that using CSW provides a sensitivity to damage up to 2.8× higher than flexural waves in the low frequency range. These results are explained by the presence of local resonances within the cross-section, producing wavelengths in the transverse direction of propagation. These waves may prove suitable for cost-effective SHM applications since they can travel long distances through heterogeneous and periodic structures.

Keywords: Elastic waves, monitoring, damage, composite, periodic, low-frequency, guided mode

1. Introduction

In the context of structural health monitoring (SHM) of composite structures, an increasing research effort was developed in recent years. The motivation is, among others, the development of non-destructive inspection techniques providing maximum information on the structural state of a specimen, as well as the possible defects localization and sizing. For this purpose, systems based on guided waves revealed very promising features and are currently used for a number of applications [1].

Email address: christophe.droz@gmail.com (C. Droz)

Yet, designing wave-based SHM systems requires effective tools for analysing and predicting the various types of elastic waves propagating in the considered structure. These waves can propagate with different group velocities, wavenumbers and spatial attenuations, and require specific actuation and measurement systems. For example, Lamb waves, originally defined for thin isotropic plates with stress-free surfaces [2], are now extensively used in SHM for anisotropic, multi-layered or other composite structures [3]. Accordingly, waveguides involving complex or heterogeneous cross-sections can produce numerous wave types, whose dispersion characteristics prediction may require advanced numerical simulation. For such applications, the Wave Finite Element Method (WFEM) uses Bloch's theorem to significantly reduce of the modelling effort. It combines Periodic Structures Theory (PST) with commercial finite element (FEM) packages and can be seen as a variant of the semi-analytical finite element (SAFE) [4, 5] method (see also the SBFEM [6]). The wave dispersion characteristics can be determined by solving a quadratic eigenvalue problem [7] obtained with a finite element model of the waveguide's cross-section.

In order to describe the wave transmission, reflection and coupling effects occurring when the aforementioned waves propagate through a defect, joint or other type of coupling element, the Diffusion Matrix Method (DMM) was developed to connect two waveguides with an elastic coupling element [8] (see [9] for similar coupling with the SAFE method). This method was extensively employed for defining reflection coefficients [10] in order to localize and evaluate cracks in pipelines [11]. The DMM is used to identify, among the different propagating wave types [8, 12], the waves which exhibit the highest sensitivity towards structural perturbation, such as reduced mass or stiffness induced by imperfection, defect or erosion. Due to the increasing requirement for more accurate inspection procedures, a number of investigations were conducted lately on the use of higher orders of Lamb wave modes to provide additional information on the type and location of defects [13, 14, 15]. One can cite for example the very recent developments on multimodal plane wave imaging technique to discriminate defects [16] and the work of Liu et al. [17] on the propagation of high-order harmonic torsional and flexural waves in circular cylinders. Interested reader may also refer to [3, 18, 19, 20] for some more recent references on the use of Lamb waves for SHM of plates.

The development of reduced wave finite element formulations also enabled fast dispersion analysis of homogeneous [21] and periodic [22] waveguides. These tools were able to observe a variety of waves in structures involving complex cross-sectional geometries [23, 24, 25]. Recently, Chillara et al. [26] proposed to use the frequency domain finite element (FDFE) technique to identify the sensitivity of several Rayleigh-Lamb waves for the detection of delaminations in a composite waveguide. Yet, the use of these waves for assessing structural integrity in composite waveguides with finite cross-section is still in its infancy.

Generally speaking, the long-range inspection of composite assemblies remains a challenge due to the important experimental noise produced by micro-structural imperfections. This issue is also observed at a smaller scale in homogeneous structures: data fusion techniques were developed for that purpose in Brierley et al [27] to reduce the probability of false alarm (PFA) for inspecting a titanium aerospace jet engine disc. Composite assemblies are even more complicated structures to inspect since they are subjected to important heterogeneities due to manufacturing imperfections periodic variations of their material properties [28, 29], producing an important number of

false calls for defect detection, while real defects are extremely rare. These structures can also be based on periodic patterns and exhibit stop-band behaviours [30] and complex scattering properties. Consequently, the SHM of structurally advanced or composites waveguides is limited to low frequency waves, providing remarkable propagating range at the cost of a reduced sensitivity to small-scaled defects. In this context, the aim of SHM is to provide informations on the integrity of a structure at a sub-system's scale, without performing inspection manually at the local component's scale.

It is emphasized that the low-frequency waves can be used for structures requiring regular or continuous monitoring, subjected to rather important alterations of their structural integrity [31] (such as the debonding of skins, a component's fracture or the effects of humidity or temperature fluctuations), given that high frequency Non-Destructive Evaluation (NDE) remains essential to detect micro-structural or small-scaled defects [32].

The aim of this work is therefore to explore the potential of high-order cross-sectional waves (CSW) to increase the sensitivity of low frequency wave-based SHM techniques. These waves are guided cross-sectional resonances propagating along the main direction, and they can be seen as a generalization of Lamb modes to waveguides involving arbitrary cross-sectional geometries. This paper addresses the diffusion of high-order guided waves through a structural singularity with the DMM. The DMM formulation is used to evaluate the reflection coefficients of different wave modes through a coupling element, while the wave dispersion characteristics are derived from the WFEM. The interactions of guided waves are compared for three different defects modelled by FEM and located at the same position. High-order wave modes, associated with increased cross-sectional strain energy are therefore in the focus of the paper. These waves are distinguished according to their dispersion characteristics and wave shapes. The WFEM and DMM formulations are reviewed in Section 2. The dispersion characteristics of uni-directional waves propagating in a sandwich plate made of transverse isotropic honeycomb core surrounded by fiber-reinforced skins are studied in Section 3. The reflection coefficients of high-order guided waves are compared through three different types of defect (Section 4) and a validation of the diffusion analysis based on time-domain simulation is finally provided in Section 5.

2. Wave propagation and diffusion through structural perturbations

2.1. Formulation of the free-wave propagation

A waveguide is considered as an elastic structure made of N identical substructures of length d, connected along the direction x. The state vector is described in figure 1. Nodal displacements and forces are denoted **q** and **f**, where the subscripts 'L' and 'R' describe the cell's left and right faces. Both edges have the same number n of degrees of freedom (DOF). Mesh compatibility is assumed between the cells. The governing equation in a cell at frequency ω is written :

$$\mathbf{Dq} = \mathbf{f} \tag{1}$$

The dynamic stiffness matrix of the unit cell $\mathbf{D} = \mathbf{K}(1 + j\eta) - \omega^2\mathbf{M}$ is obtained using standard finite element packages, where $\mathbf{K}$ denotes the stiffness matrix, $\mathbf{M}$ is the mass matrix and η is the

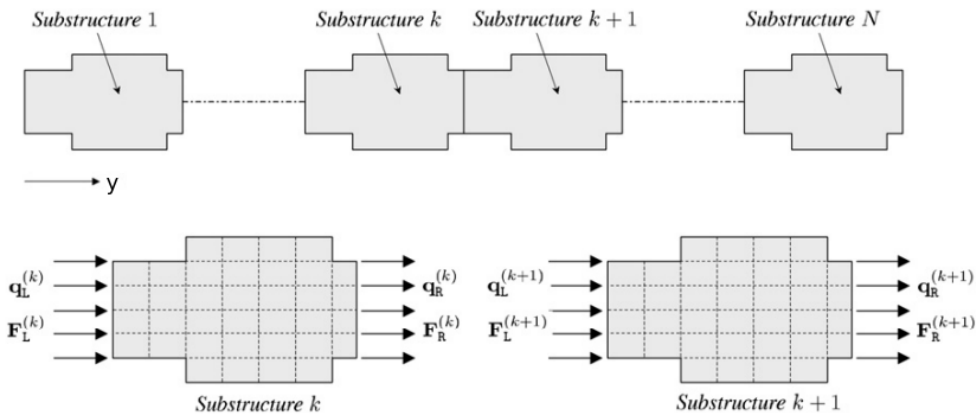

Figure 1: Illustration of a waveguide and the state vector of a unit cell. d is the length of the unit-cell in the x-direction.

structural loss factor. Then, a dynamic condensation of the inner DOF is recommended if the structure is periodic. The governing equation can be written by separating the degrees of freedom on the right and left edges :

$$\begin{bmatrix} \mathbf{D}_{LL} & \mathbf{D}_{LR} \\ \mathbf{D}_{RL} & \mathbf{D}_{RR} \end{bmatrix} \begin{Bmatrix} \mathbf{q}_L \\ \mathbf{q}_R \end{Bmatrix} = \begin{Bmatrix} \mathbf{f}_L \\ \mathbf{f}_R \end{Bmatrix}. \tag{2}$$

Then, considering the force equilibrium in a cell $\lambda \mathbf{f}_L + \mathbf{f}_R = 0$ and Bloch's theorem [33] $\mathbf{q}_R = \lambda \mathbf{q}_L$, where the propagation constant $\lambda = e^{-jkd}$ describes the wave propagation over the cell length d with the wavenumber k, it yields the following quadratic eigenproblem :

$$\mathbf{S}(\lambda, \omega) = (\lambda \mathbf{D}_{LR} + (\mathbf{D}_{LL} + \mathbf{D}_{RR}) + \frac{1}{\lambda}\mathbf{D}_{RL})\mathbf{q}_L = \mathbf{0} \tag{3}$$

where the eigenvectors stand for the wave shape associated with the displacements $\mathbf{q}_L$ of the waveguide's cell. Whether material damping is modelled or not, the imaginary part of a wavenumber $\Im(k)$ describes wave attenuation. Here, the waves associated with positive real wavenumber $\Re(k)$ are travelling in the positive x-direction and the negative wavenumbers describe propagation in the negative x-direction.

The displacements $q_L^{(k)}$ and $q_R^{(k)}$ of any substructure k can be written using the wave solutions of Eq.(3) $\{\mathbf{\Phi}_i\}_{i=1,\dots,2n}$:

$$q_L^{(k)} = \mathbf{\Phi}\mathbf{Q}^{(k)} \quad , \quad q_R^{(k)} = \mathbf{\Phi}\mathbf{Q}^{(k+1)} \tag{4}$$

where the wave solutions $\mathbf{\Phi}$ can be ordered as follows:

$$\mathbf{\Phi} = \begin{bmatrix} \mathbf{\Phi}_{\mathbf{q}}^{\mathtt{inc}} & \mathbf{\Phi}_{\mathbf{q}}^{\mathtt{ref}} \\ \mathbf{\Phi}_{\mathbf{F}}^{\mathtt{inc}} & \mathbf{\Phi}_{\mathbf{F}}^{\mathtt{ref}} \end{bmatrix}, \tag{5}$$

where `inc` refers to the incident waves and `ref` denotes the reflected waves, while the vector $\mathbf{Q}$ stands for the wave amplitudes, written:

$$\mathbf{Q} = \begin{pmatrix} \mathbf{Q}^{\mathtt{inc}} \\ \mathbf{Q}^{\mathtt{ref}} \end{pmatrix}. \tag{6}$$

These wave amplitudes can therefore be used for the determination of transmitted and reflected waves amplitudes through a coupling element.

2.2. Wave diffusion through a coupling element

Consider the two waveguides connected with an elastic coupling element in figure 2. The substructures are connected, assuming compatible mesh at the interfaces Γ_1 and Γ_2 and no external forces are applied on the coupling element.

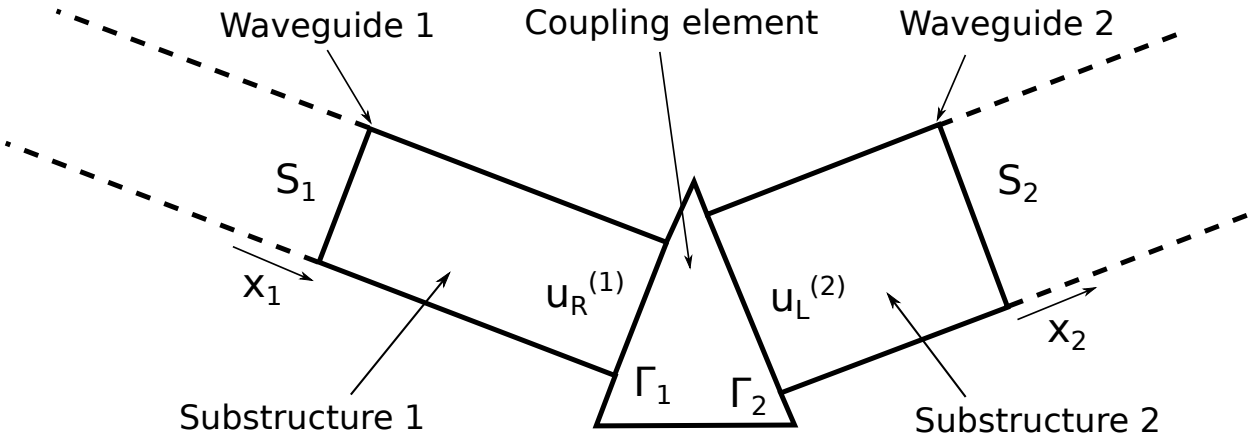

Figure 2: Diagram describing the coupling between two waveguides. The coupling element is defined by a sandwich plate section where the considered defect is included.

The condensed dynamical stiffness of the coupling element is denoted $\mathbb{D}^*_c$. Therefore, considering the relations between the displacements $(\mathbf{q}_{\mathrm{R}}^{(1)}, \mathbf{q}_{\mathrm{L}}^{(2)})$ and the forces $(\mathbf{F}_{\mathrm{R}}^{(1)}, \mathbf{F}_{\mathrm{L}}^{(2)})$ applied on the surfaces Γ_1 and Γ_2 the coupling relation between the two waveguides can be written :

$$\mathbb{D}^{c*} \begin{pmatrix} \mathbf{q}_{\mathrm{R}}^{(1)} \\ \mathbf{q}_{\mathrm{L}}^{(2)} \end{pmatrix} = \begin{pmatrix} \mathbf{F}_{\mathrm{R}}^{(1)} \\ \mathbf{F}_{\mathrm{L}}^{(2)} \end{pmatrix}. \tag{7}$$

The dynamical behaviour of the coupled waveguide can be described using the incident $((\mathbf{\Phi}_{\mathbf{q}}^{\mathtt{inc}(i)})^{\mathtt{T}}(\mathbf{\Phi}_{\mathbf{F}}^{\mathtt{inc}(i)})^{\mathtt{T}})^{\mathtt{T}}$ and reflected $((\mathbf{\Phi}_{\mathbf{q}}^{\mathtt{ref}(i)})^{\mathtt{T}}(\mathbf{\Phi}_{\mathbf{F}}^{\mathtt{ref}(i)})^{\mathtt{T}})^{\mathtt{T}}$ waves given by Eq.(5) . Therefore, it can be shown in reference [8] that the incident $(\mathbf{Q}^{\mathtt{inc}(1)}, \mathbf{Q}^{\mathtt{inc}(2)})$ and reflected $(\mathbf{Q}^{\mathtt{ref}(1)}, \mathbf{Q}^{\mathtt{ref}(2)})$ wave amplitudes are related through a diffusion matrix $\mathbb{C}$:

$$\begin{pmatrix} \mathbf{Q}^{\mathtt{ref}(1)} \\ \mathbf{Q}^{\mathtt{ref}(2)} \end{pmatrix} = \mathbb{C} \begin{pmatrix} \mathbf{Q}^{\mathtt{inc}(1)} \\ \mathbf{Q}^{\mathtt{inc}(2)} \end{pmatrix}, \tag{8}$$

where the diffusion matrix $\mathbb{C}$ is expressed (see [8]) in terms of the incident and reflected wave solutions described in Eq.(5). In the following section, the diffusion matrix $\mathbb{C}$ is determined to provide the transmission `t` and reflection `r` coefficients of CSW in a sandwich waveguide exhibiting structural perturbations.

3. Guided CSW in the sandwich plate

The considered waveguide is a rectangular and symmetric sandwich plate, composed of a 8 mm thick homogenised honeycomb core surrounded by 1 mm thick fibre-reinforced skins (see [34] for example of more complex geometrical models). The 400 mm width cross-section is modelled

on ANSYS V12.1 and convergence is ensured within the considered frequency range by using 360 linear brick elements having 8-nodes and 3 degrees of freedom (DOF) per node. A detailed description of the materials is given in tables 1 and 2.

Material	Density (kg.m^{-3})	Young Modulus (Pa)	Shear Modulus (Pa)
Core	24	$E_x = 5 \times 10^6$ $E_y = 5 \times 10^6$ $E_z = 46.6 \times 10^6$	$G_{xy} = 1 \times 10^6$ $G_{xz} = 10.13 \times 10^6$ $G_{yz} = 10.13 \times 10^6$

Table 1: Material properties of the transverse isotropic honeycomb core (from [35]).

Material	Density (kg.m^{-3})	Young Modulus (Pa)	Shear Modulus (Pa)
Skins	1451	$E_x = 81 \times 10^9$ $E_y = 81 \times 10^9$ $E_z = 3.35 \times 10^9$	$G_{xy} = 2.5 \times 10^9$ $G_{xz} = 2.8 \times 10^9$ $G_{yz} = 2.8 \times 10^9$

Table 2: Material properties of the transverse isotropic fiber-reinforced skins (from [35]).

The wave dispersion characteristics of the sandwich structure are given in figure 3. Continuous lines describe first-order waves while dashed lines represent high-order CSW. The flexural waves are distinguished using a wave-matching procedure. At each frequency step, the solution is compared to the whole set of propagating waves using a Wave Assurance Criterion (WAC) [22]. A unique wave can be defined at two consecutive frequencies when the orthogonality condition between two cross-sectional deformed shapes $\Psi(\omega_i)$ and $\Psi(\omega_j)$ is above a threshold $\varepsilon \in [0\,,\,1]$.

The real wavenumbers and group velocities of propagating waves are shown in figure 3.a. In the considered waveguide, high-order waves appearing in the frequency range 0 Hz – 5000 Hz are propagating solutions associated with sinusoidal cross-sectional shapes. The solutions for the 3^{rd} and 10^{th} orders are shown in figures 4.a and 4.b. An additional CSW, associated with symmetric deformed shape (appearing in higher frequency) is illustrated in figure 4.c. Although the solutions (a) and (b) are referred as high-order CSW, they share the same asymptotic group velocity of the first-order flexural wave.

4. Sensitivity to localized structural singularity

4.1. Description of the defects

In this section, a diffusion analysis based on the results from section 3 is conducted in the sandwich waveguide, assuming three different defect types. The skin, core defects and delamination are modelled using 3D finite elements and are located at the same position on the plate. The two 'defect free' domains are therefore connected by a coupling element defined as a section of plate involving a defect. The three finite element models of the defects described in Figure 5 are therefore considered as the coupling elements for the DMM. The skin and core defects are simplified, and defined by a local reduction of their isotropic Young's and Shear coefficients $(G, E) \rightarrow 0$,

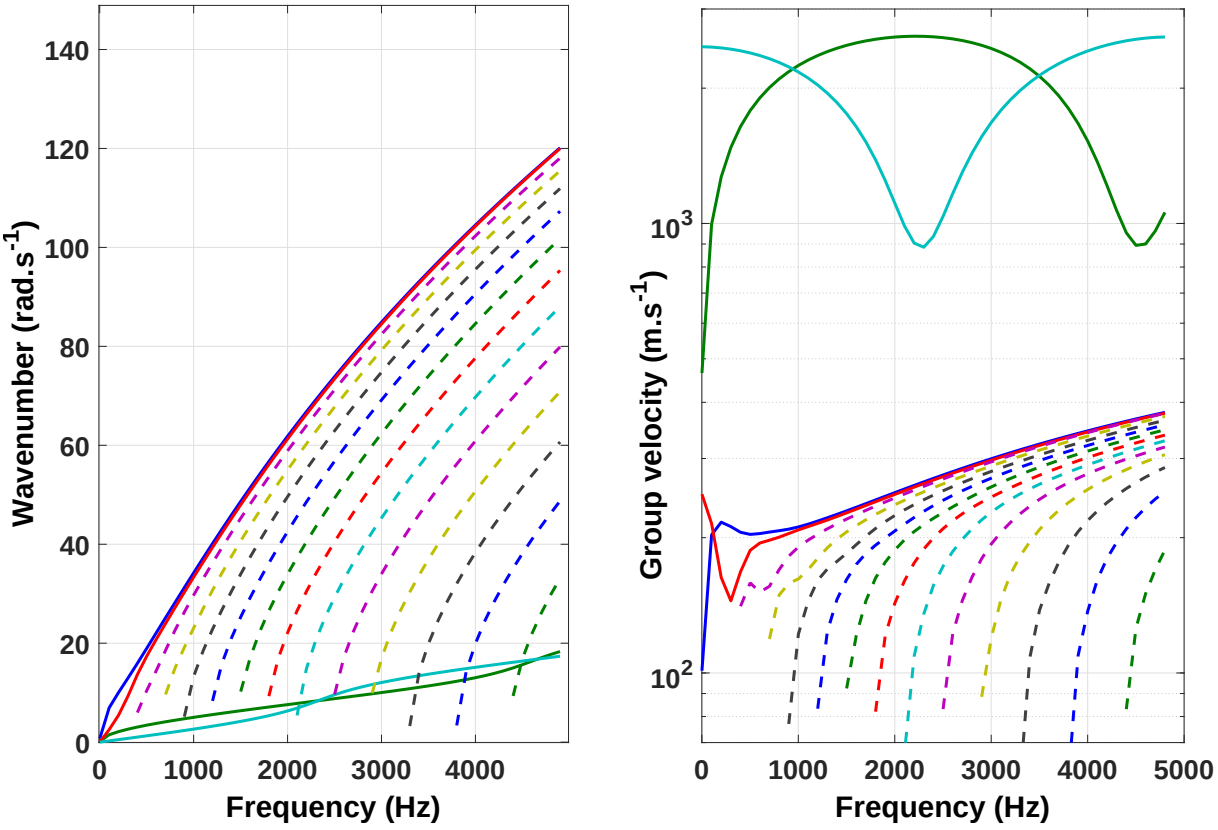

Figure 3: Wavenumbers (a) and group velocities (b) of propagating, positive-going waves along the main direction x. Continuous lines are used for flexural, torsional, longitudinal and shear waves while dashed lines refer to high-order waves.

while the idealized delamination is defined by a disconnection between the skin and core layers. The dimensions of the three defects is $l_x \times l_y = 10 \times 46$ mm and their location on the cross-section is defined by $Y_0 = 160$ mm.

4.2. Effects on reflection coefficients

Note that the forced response calculation and CSW actuation are not required here for the diffusion analysis. Indeed, the diffusion matrix introduced in Eq.(8) provides the reflection, transmission and conversion coefficients of guided waves through the coupling elements described above. Since the sandwich structure exhibits more than 16 waves in the considered frequency range and for a sake of clarity, only five waves are studied in detail. The reflection coefficients of the first-order waves through the defects is shown between 1 kHz and 6 kHz in figure 6.a while the reflection of higher wave orders is shown in figure 6.b. A computation was also conducted without defects to ensure that energy balance is satisfied (see Section 5).

First-order waves exhibit a maximal reflection of 4 % at 6 kHz, while the 2^{nd}-order reaches 10.7 % at the same frequency for the skin defect. It is reminded that the use of low-frequency waves for SHM is characterized by a reduced sensitivity to small-scaled singularities. CSW are therefore

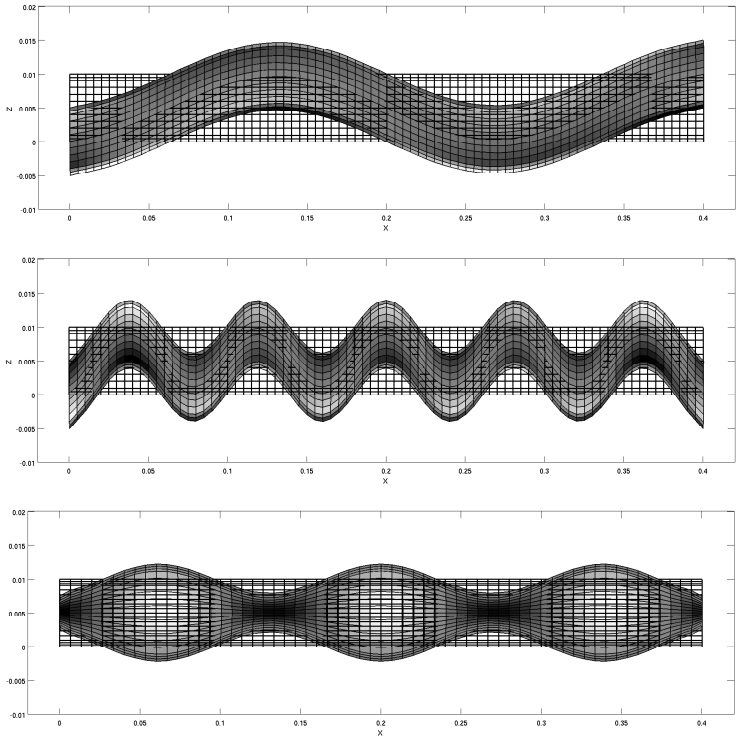

Figure 4: Deformed shapes of three propagating waves associated with cross-sectional modes. 3^{rd}-order wave (a), 10^{th}-order wave (b) and 6^{th}-order symmetric wave. The three solutions are shown at their cut-on frequency.

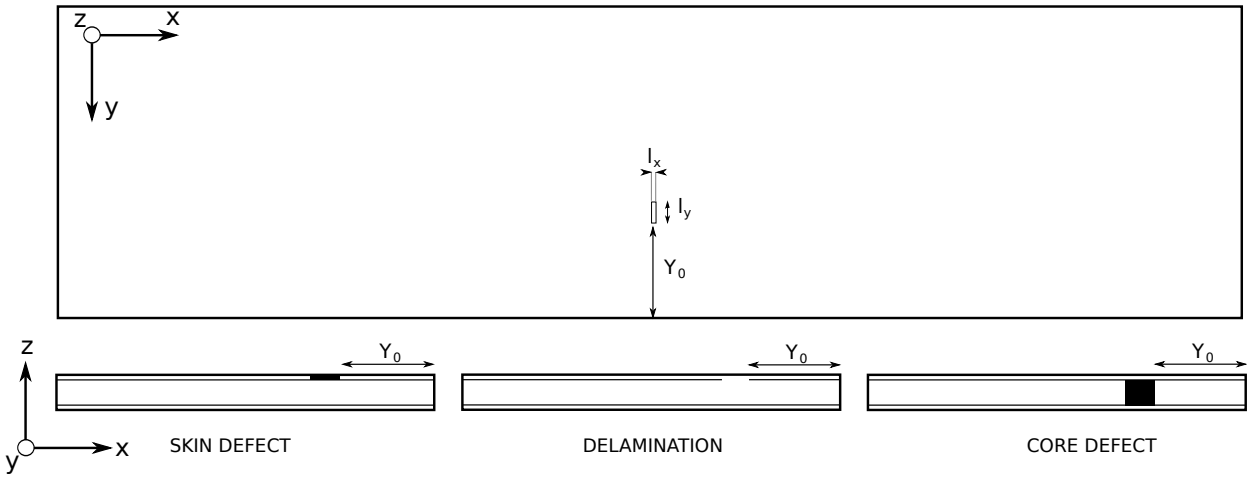

Figure 5: Location of the three defects considered in the sandwich structure. (a) Skin defect. (b) Delamination of the upper skin. (c) Core defect.

expected to produce higher reflection coefficients when the singularity alters the propagation in the transverse direction of propagation. The skin and core defects and delamination are described using markers and show that the defects cannot be distinguished from each other using first-order waves reflections. On the other hand, the reflections of 2^{nd}-, 4^{th}- and 8^{th}-orders clearly differ with

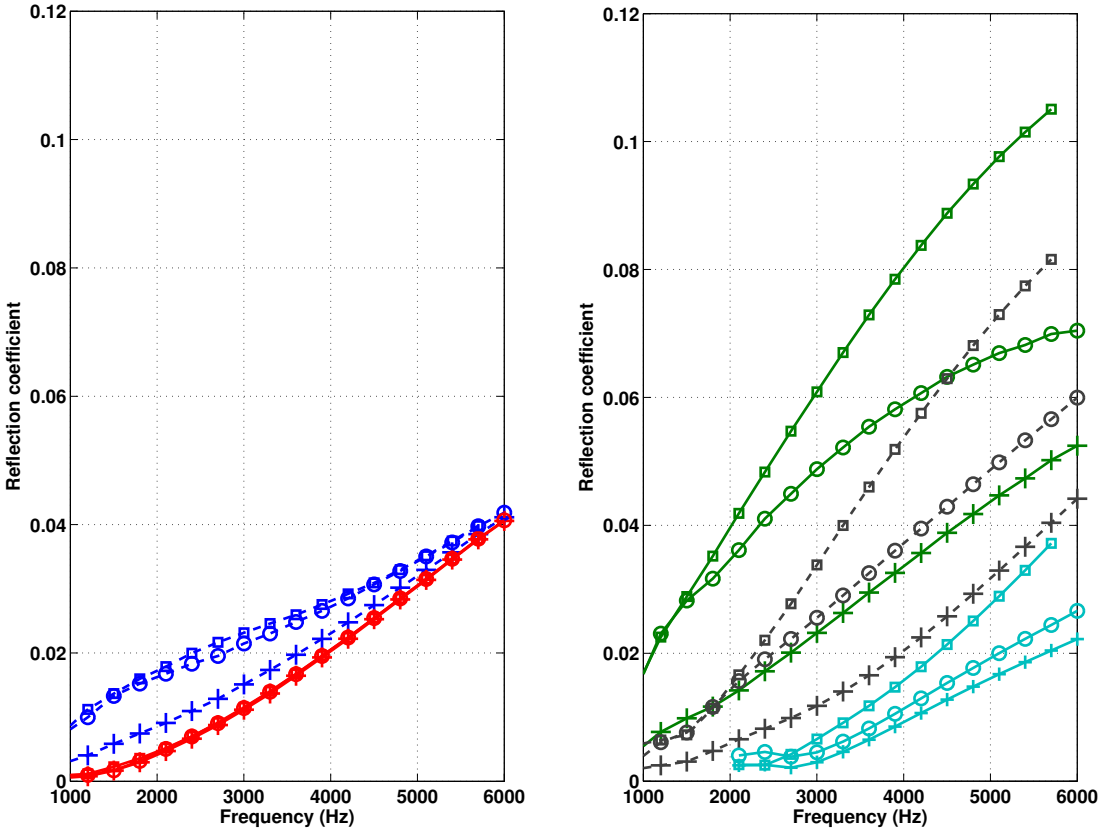

Figure 6: Reflection coefficients of the first-order flexural (- - -) and torsional (——) waves (a) and the 2^{nd}-order (——), 4^{th}-order (- - -) and 8^{th}-order (——) waves (b). Markers are used to discriminate delamination model (+) and the defects located in the skin (□) and the core (○).

the defect type. For example, the 4^{th}-order wave has an approximate reflection of 3 %, 5 % and 7 % on the delamination, core and skin defects, respectively.

4.3. Discussions

Noteworthy, the reflection of high-order CSW increase more rapidly with frequency, despite they are null around their cut-on frequencies. This can be explained by considering the two underlying effects producing wave reflection: one is directly related to the wavelength λ_x in the direction of propagation, while the second one is due to the presence of a wavelength λ_y in the transverse direction of propagation. The reflection of high-order CSW is due to this second effect.

However, the use of guided waves close to their cut-on frequency has several disadvantages. Firstly, since a wave attenuation is written [36]:

$$\gamma = \frac{\pi\omega\eta}{2c_g} \tag{9}$$

where η is the structural loss factor, then low group velocities c_g occuring close to CSW's cut-on are expected to produce slightly higher spatial attenuation of the waves than first-order CSW. The second drawback is due to the important variations of the group velocities, producing significant dispersive behaviour [37]. Indeed, a finite width time-domain excitation pulse produces a broadband spectrum, leading to important variations of the energy velocity around these cut-on frequencies. Although the dispersion effects are not taken into account by the proposed diffusion analysis, it should be mentioned that the DMM is highly competitive compared to virtual testing for analysing high-order waves diffusion through defects.

It can further be observed that the CSW reflections shown in figure 6 remain below 11 % in the considered frequency range. Note that these values would be too low in the context of a high frequency NDE approach, since experimental errors and noise-to-signal ratio would then be to important. The authors emphasize that the use of low frequency waves at high amplitudes provides significant reduction of the relative noise, thus making it possible to use the reflected signal for practical applications.

5. Comparison with time-domain results

In this section, the results of the diffusion analysis are compared with the reflection and transmission of CSW of the sandwich structure to a wave pulse in the time domain.

5.1. Time-analysis and excitation signal

Numerical simulations are conducted hereby to evaluate the reflected and transmitted signals through the three structural singularities described in the previous section. Each solution presented in figure 6 represents the reflection coefficient of a unique wave type propagating at a given frequency through a single defect. The procedure for evaluating the reflection of the 4^{th}-order wave at 3500 Hz on the core's defect is detailed below. First, the structure is modelled using the material characteristics described in tables 1 and 2 with the commercial finite element analysis package ABAQUS CAE V6.13. Conservative FE meshes involving at least 20 elements per wavelength were used for each simulation to ensure convergence. The defect is defined as shown in figure 5 and located at a distance $X_0 = 2000$ mm from the edge.

The excitation signal is a tone burst involving 10 cycles and a total duration $T = 2.86$ ms. Since the number of cycles influences the bandwidth of the excitation spectrum, the condition of existence of a 4^{th}-order cross-sectional mode in the frequency bandwidth is verified in figure 7. It can be seen that the values of the wavenumbers, energy velocity and reflection coefficients obtained from the transient response can be subjected to significant variations in case of an increased number of pulse cycles.

Different wave types are actuated by applying the Dirichlet conditions at the boundary $x = 0$ (left side in figures 5 and 8) and the maximal pulse amplitude is $U_0 = 50\,\mu$m. The finite element model employs 378,800 linear C3D8 elements and is solved using Abaqus/Explicit solver. The propagation of the 4^{th}-order wave pulse at 3500 Hz in the sandwich and the reflection on the core's defect is shown in figure 8. Note that the mesh density is increased at higher frequency to ensure convergence as the wavelength becomes smaller. The reflected pulse can be observed on step 3. It can be seen from the three time steps that the diffusion of the wave pulse is associated with conversion effects, producing an increased dispersion of the reflected pulse.

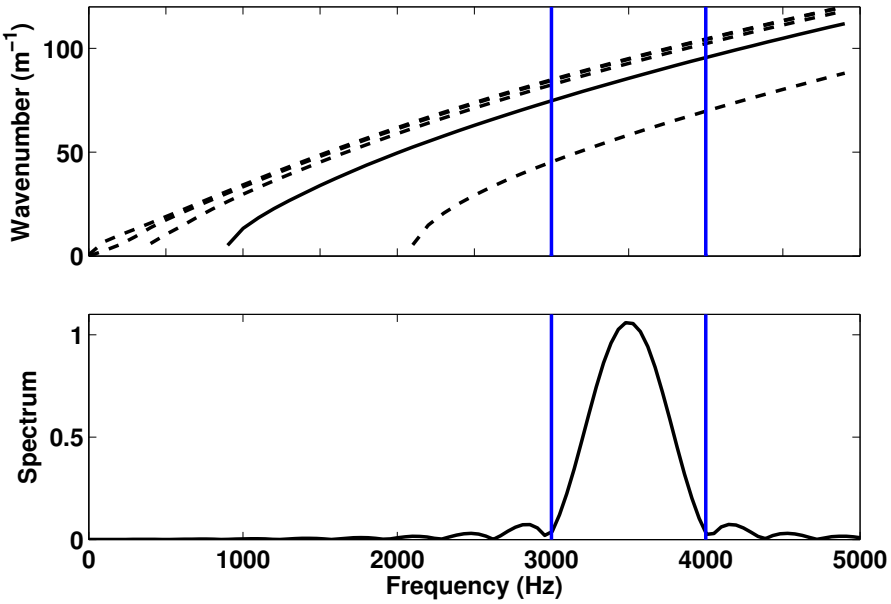

Figure 7: Dispersion curves of the 4^{th}-order wave (——) and others (- - -) between 0 and 5 kHz (a). Frequency spectrum of the tone burst centred at 3500 Hz (b). Contributions of the excitation signal in the frequency domain are expected between 3 kHz and 4 kHz (vertical ——).

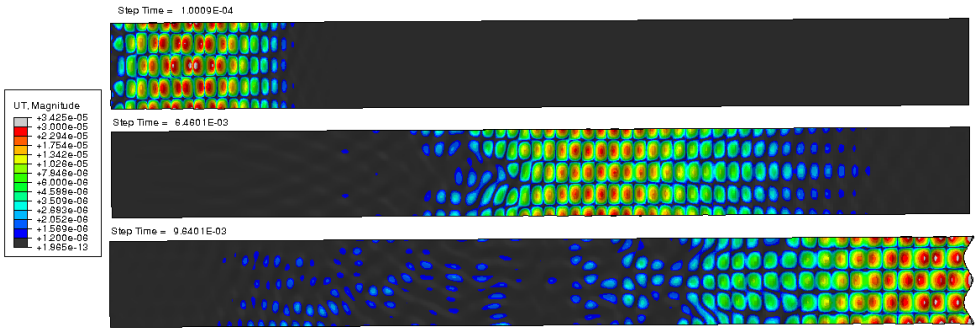

Figure 8: Propagation of a 4^{th}-order wave pulse at 3500 Hz in the sandwich plate (a) and diffusion through a defect located in the core (b and c). Total length is 5 m. Colormap: normal surface amplitudes in logarithmic scale. FEM involves 8 elements in the core's thickness and 120 elements in the width.

5.2. Computation of the wave pulse reflection

Since the propagation involves a complex cross-sectional displacement field, the diffusion cannot be defined in terms of transmitted and reflected amplitudes on a single degree of freedom. Cross-sectional energies are therefore employed below. The velocities are acquired on the sections located at $X_1 = 100$ mm and $X_2 = 2300$ mm, denoted $\mathbf{v}(X_1, y, z, t)$ and $\mathbf{v}(X_2, y, z, t)$. We denote $\mathbf{V}_i\{y, z\}(t)$ the Hilbert Transform of the velocity $\mathbf{v}(X_i, y, z, t)$ and $\rho(y, z)$ the density on a section of

the plate. The instantaneous cross-sectional energy is written:

$$\mathbf{E}_i(t) = \iint_S \frac{1}{2}\rho(y,z)\left|\mathbf{V}_i^2\{y,z\}(t)\right| \,\mathrm{d}y\,\mathrm{d}z \tag{10}$$

where $\rho(y,z)$ is the section density.

The normal velocities at the section location $y = Y_0$ and their Hilbert envelope are shown for the incident and transmitted wave pulse in figure 9. The reflected pulse on the defect can be seen on X_1 at $t = 14\,\mathrm{ms}$. A small dispersion of the wave pulse is also observed, although it should be noted that a numerical dispersion can occur and damping is not taken into account here.

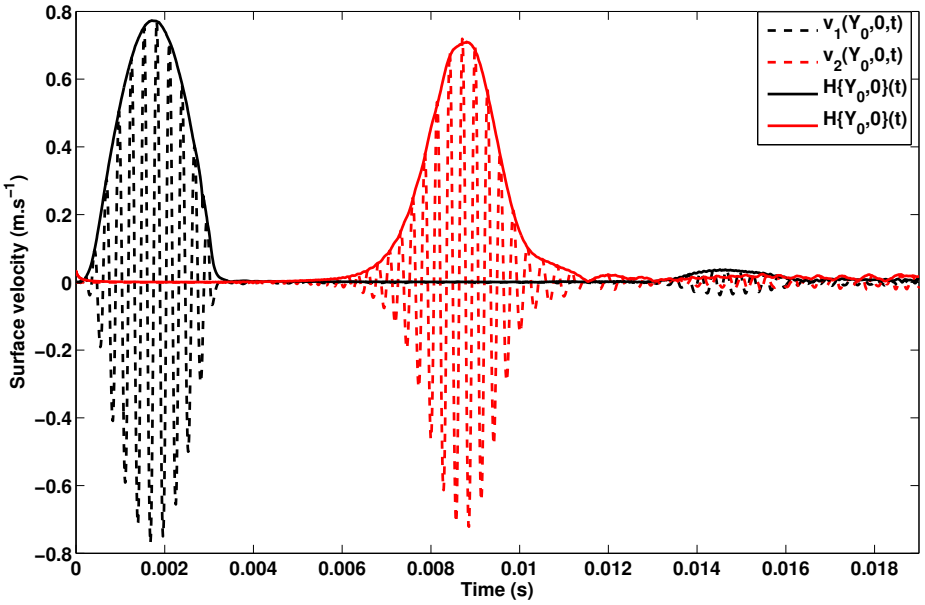

Figure 9: Time acquisition at $Y_0 = 0.2\,\mathrm{m}$, under a 4^{th}-order wave pulse at 3500 Hz at locations X_1 and X_2 (**- - -**) and Hilbert envelope (——).

The transmission coefficient is expressed in terms of the cumulated cross-sectional energy of the wave pulse:

$$\mathbf{C_t} = 1 - \mathbf{C_r} = \frac{< E_2 >}{< E_1 >} \tag{11}$$

where $< E_i >= \int_{t\in T_i} E_i(t)\,\mathrm{d}t$ and T_i is a time window of the wave pulse. It is defined using the threshold $\varepsilon = 1\%$ by $E_i(t) < \varepsilon \max_t(E_i)$. This threshold is commonly employed to define the pulse duration while accounting for potential dispersion or noise, although more accurate techniques based on the computation of dispersion curves could be used here (see Wilcox [37] for example). The results summarized in table 3 show that the ratio of maximal energy values produce a clear underestimation of the reflection coefficient (<0.87%) while the time-integrated pulse is in good agreement with the DMM predictions ($\mathbf{C_r} = 3.14\,\%$). It can be explained by the spatial dispersion of the wave pulse, which is independent from the spatial attenuation.

Core's defect	$\max_t(E_1)$ (J.m^{-1})	$\max_t(E_2)$ (J.m^{-1})	$< E_1 >$ (J.m^{-1}.s)	$< E_2 >$ (J.m^{-1}.s)	**r** (%)
4^{th} wave at 3500 Hz	8.02 10^{-5}	7.95.10^{-5}	1.85^{-4}	1.79^{-4}	**3.52**

Table 3: Energy calculations for the 4^{th} wave reflection on a core type defect at 3500 Hz.

5.3. Discussions

The procedure described above is conducted for other waves and defects types, while the reflection coefficients determined using Eq. (11) are summarized in table 4. The results are in very good agreement with the DMM predictions presented in figure 6. Noteworthy, the reflection coefficients are in the same order for the four excitation cases:

$$\mathbf{C_r^{skin}} < \mathbf{C_r^{core}} < \mathbf{C_r^{debond}} \tag{12}$$

Wave	Frequency (Hz)	Skin (%)	Core (%)	Debond (%)
0^{th}-order	3000	**2.83**	**2.69**	**1.50**
2^{nd}-order	1500	**3.10**	**2.98**	**1.13**
4^{th}-order	2500	**2.64**	**2.16**	**1.29**
4^{th}-order	3500	**4.61**	**3.52**	**2.09**

Table 4: Reflection coefficients through the each defect, obtained for different wavetypes and frequencies.

The values are also close to the ones obtained by diffusion analysis, although they are slightly overestimated. For example, the skin defect gives a 2.64 % reflection for a 4^{th} at 2500 Hz, while the diffusion analysis predicts a 2.39 % reflection. Similarly, the same wavetype at 3500 Hz gives a 4.61 % reflection by simulation, against 4.39 % with the DMM. The wave conversion through the defect is most likely to be the main reason for this, given that the reflection coefficients obtained through averaged cross-sectional energies do not discriminate between the reflected wavetypes.

Indeed, the total cross-sectional energy reflected and transmitted through the coupling element is the sum of the contributions from all the wavetypes, and is written:

$$\mathbf{C_r} = \mathbf{C_r^{j\to j}} + \sum_{i\neq j} \mathbf{C_r^{j\to i}} \quad \text{and} \quad \mathbf{C_t} = \mathbf{C_t^{j\to j}} + \sum_{i\neq j} \mathbf{C_t^{j\to i}} \tag{13}$$

where the coefficients $\mathbf{C^{i\to j}}$ denote the wave amplitudes of type i resulting from the conversion of wavetype j. Since the DMM gives the $\mathbf{C_r^{j\to j}}$ values, it is likely that the increased reflection values observed in simulation are due to the converted waves $\left\{\mathbf{C_r^{j\to i}}\right\}_{i\neq j}$.

Although the proposed validation model would certainly benefit from a filtering procedure based on WAC to estimate accurately the coefficient $\mathbf{C_r^{j\to j}}$, it is emphasized that the computation of reflection coefficients based on FEM simulation involves considerable computation time compared to diffusion analysis.

6. Concluding remarks

The paper describes an original way of using high-order cross-sectional waves (CSW) to increase the sensitivity of low-frequency guided wave techniques for the SHM of a sandwich plate with finite section. The sandwich plate considered in this work exhibits numerous wavetypes associated with complex mode shapes of the cross-section. Although these waves are known to exhibit slightly higher spatial attenuations in dissipative waveguides at a given frequency, they propagate over long distances through heterogeneous or composite waveguides due to their low frequencies, and with comparable dispersion characteristics with first-order waves above their cut-on frequency.

A diffusion analysis was conducted through three types of defects (skin, core and delamination), and demonstrated that a waveguide's finite section could be seen as an opportunity to exploit the reflection characteristics of CSW. These waves produce higher reflection coefficients and provide additional informations on a given structural singularity. This property was observed for five different wave types up to 5 kHz, which corresponds to a medium frequency range for the considered structure. The increased reflections of CSW on a defect can be explained by the presence of a reduced wavelength in the transverse direction of propagation, possibly further enabling the detection of a longitudinal crack along the direction of propagation. The authors are not aware of a comparable use of CSW having been proposed elsewhere for the structural integrity assessment of structures. The results detailed in section 5 show that a time-domain simulation can be compared with the DMM, assuming that the classical conditions of a monochromatic propagating pulse are met. The conducted simulations confirm that CSW can be actuated by applying the proper boundary conditions. The utility of a spectral DMM was also highlighted for estimating their reflections on various defects using the dispersion characteristics, although other methods can be found in the literature (see [38]).

Finally, it should be mentioned that the present analysis has been concerned with a symmetric sandwich plate involving homogeneity along the width. It is likely that mode conversion or localisation effects will occur through more complex cross-sections, even though the numerical approach employed in the paper remains the same. In that case, the concept of leaky waves between the different structural components would also be applicable [39, 40]. For a "conventional" sandwich plate with a finite section, the present analysis shows that cross-sectional waves can be seen as a potential solution to improve the sensitivity of low-frequency guided wave techniques for SHM.

References

[1] Rose, J.L.. Ultrasonic guided waves in structural health monitoring. In: Key Engineering Materials; vol. 270. Trans Tech Publ; 2004, p. 14–21.

[2] Lamb, H.. On waves in an elastic plate. Proceedings of the Royal Society of London Series A, Containing papers of a mathematical and physical character 1917;:114–128.

[3] Sikdar, S., Banerjee, S., Ashish, G.. Ultrasonic guided wave propagation and disbond identification in a honeycomb composite sandwich structure using bonded piezoelectric wafer transducers. Journal of Intelligent Material Systems and Structures 2015;:1045389X15610906.

[4] Hayashi, T., Song, W.J., Rose, J.L.. Guided wave dispersion curves for a bar with an arbitrary cross-section, a rod and rail example. Ultrasonics 2003;41(3):175–183.

[5] Hayashi, T., Kawashima, K., Sun, Z., Rose, J.L.. Analysis of flexural mode focusing by a semianalytical finite element method. The Journal of the Acoustical Society of America 2003;113(3):1241–1248.
[6] Gravenkamp, H., Prager, J., Saputra, A.A., Song, C.. The simulation of lamb waves in a cracked plate using the scaled boundary finite element method. The Journal of the Acoustical Society of America 2012;132(3):1358–1367.
[7] Mace, B.R., Duhamel, D., Brennan, M.J., Hinke, L.. Finite element prediction of wave motion in structural waveguides. J Acous Soc Am 2005;117:2835–2843.
[8] Ichchou, M., Mencik, J.M., Zhou, W.. Wave finite elements for low and mid-frequency description of coupled structures with damage. Computer methods in applied mechanics and engineering 2009;198(15):1311–1326.
[9] Ahmad, Z., Gabbert, U.. Simulation of lamb wave reflections at plate edges using the semi-analytical finite element method. Ultrasonics 2012;52(7):815–820.
[10] Renno, J.M., Mace, B.R.. Calculation of reflection and transmission coefficients of joints using a hybrid finite element/wave and finite element approach. Journal of Sound and Vibration 2013;332(9):2149–2164.
[11] Bareille, O., Kharrat, M., Zhou, W., Ichchou, M.N.. Distributed piezoelectric guided-t-wave generator, design and analysis. Mechatronics 2012;22:544–551.
[12] Droz, C., Lainé, J.P., Ichchou, M., Inquiété, G.. A reduced formulation for the free-wave propagation analysis in composite structures. Compos Struct 2014;113:134–144.
[13] Watkins, R., Jha, R.. A modified time reversal method for lamb wave based diagnostics of composite structures. Mechanical Systems and Signal Processing 2012;31:345 – 354.
[14] Ostachowicz, W., Kudela, P., Malinowski, P., Wandowski, T.. Damage localisation in plate-like structures based on pzt sensors. Mechanical Systems and Signal Processing 2009;23(6):1805–1829.
[15] Balasubramaniam, K., et al. Lamb-wave-based structural health monitoring technique for inaccessible regions in complex composite structures. Structural Control and Health Monitoring 2014;21(5):817–832.
[16] Le Jeune, L., Robert, S., Villaverde, E.L., Prada, C.. Plane wave imaging for ultrasonic non-destructive testing: Generalization to multimodal imaging. Ultrasonics 2016;64:128–138.
[17] Liu, Y., Khajeh, E., Lissenden, C.J., Rose, J.L.. Higher order interaction of elastic waves in weakly nonlinear hollow circular cylinders. ii. physical interpretation and numerical results. Journal of Applied Physics 2014;115(21).
[18] Baid, H., Schaal, C., Samajder, H., Mal, A.. Dispersion of lamb waves in a honeycomb composite sandwich panel. Ultrasonics 2015;56:409–416.
[19] Levine, R.M., Michaels, J.E.. Block-sparse reconstruction and imaging for lamb wave structural health monitoring. IEEE transactions on ultrasonics, ferroelectrics, and frequency control 2014;61(6):1006–1015.
[20] Dodson, J., Inman, D.. Thermal sensitivity of lamb waves for structural health monitoring applications. Ultrasonics 2013;53(3):677–685.
[21] Mencik, J.M.. A model reduction strategy for computing the forced response of elastic waveguides using the wave finite element method. Comput Methods Appl Mech Eng 2012;229–232:68–86.
[22] Droz, C., Zhou, C., Ichchou, M., Lainé, J.P.. A hybrid wave-mode formulation for the vibro-acoustic analysis of 2d periodic structures. Journal of Sound and Vibration 2016;363:285–302.
[23] Huang, T., Ichchou, M., Bareille, O.. Multi-mode wave propagation in damaged stiffened panels. Structural Control and Health Monitoring 2012;19(5):609–629.
[24] Nguyen, K., Treyssède, F.. Numerical investigation of leaky modes in helical structural waveguides embedded into a solid medium. Ultrasonics 2015;57:125–134.
[25] Li, F., Sun, X., Qiu, J., Zhou, L., Li, H., Meng, G.. Guided wave propagation in high-speed train axle and damage detection based on wave mode conversion. Structural Control and Health Monitoring 2015;22(9):1133–1147.
[26] Chillara, V.K., Ren, B., Lissenden, C.J.. Guided wave mode selection for inhomogeneous elastic waveguides using frequency domain finite element approach. Ultrasonics 2015;.
[27] Brierley, N., Tippetts, T., Cawley, P.. Data fusion for automated non-destructive inspection. In: Proc. R. Soc. A; vol. 470. 2014, p. 20140167.
[28] Scarpa, F., Ouisse, M., Collet, M., Saito, K.. Kirigami auxetic pyramidal core: mechanical properties and wave propagation analysis in damped lattice. Journal of Vibration and Acoustics 2013;135(4):041001.

[29] Chronopoulos, D.. Design optimization of composite structures operating in acoustic environments. Journal of Sound and Vibration 2015;355:322–344.
[30] Xiao, Y., Mace, B.R., Wen, J., Wen, X.. Formation and coupling of band gaps in a locally resonant elastic system comprising a string with attached resonators. Physics Letters A 2011;375(12):1485–1491.
[31] Giurgiutiu, V., Bao, J.. Embedded-ultrasonics structural radar for in situ structural health monitoring of thin-wall structures. Structural Health Monitoring 2004;3(2):121–140.
[32] Alleyne, D.N., Cawley, P.. The interaction of lamb waves with defects. IEEE transactions on ultrasonics, ferroelectrics, and frequency control 1992;39(3):381–397.
[33] Bloch, F.. Über die quantenmechanik der elektronen in kristallgittern. Zeitschrift für physik 1929;52(7-8):555–600.
[34] Hosseini, S.M.H., Gabbert, U.. Numerical simulation of the lamb wave propagation in honeycomb sandwich panels: a parametric study. Composite Structures 2013;97:189–201.
[35] Droz, C.. High-order wave propagation in composite waveguides: application to in-flight de-icing of helicopter rotor blades. Ph.D. thesis; École Centrale de Lyon; 2015.
[36] Lyon, R.H., DeJong, R.G., Heckl, M.. Theory and application of statistical energy analysis. J Acous Soc Am 1995;98:3021.
[37] Wilcox, P.D.. A rapid signal processing technique to remove the effect of dispersion from guided wave signals. IEEE transactions on ultrasonics, ferroelectrics, and frequency control 2003;50(4):419–427.
[38] Rodriguez, S., Deschamps, M., Castaings, M., Ducasse, E.. Guided wave topological imaging of isotropic plates. Ultrasonics 2014;54(7):1880–1890.
[39] Castaings, M., Lowe, M.. Finite element model for waves guided along solid systems of arbitrary section coupled to infinite solid media. The Journal of the Acoustical Society of America 2008;123(2):696–708.
[40] Treyssede, F., Nguyen, K.L., Bonnet-BenDhia, A.S., Hazard, C.. Finite element computation of trapped and leaky elastic waves in open stratified waveguides. Wave Motion 2014;51(7):1093–1107.